

Chemical Mixing Induced by Internal Gravity Waves in Intermediate Mass Stars

A. VARGHESE,¹ R. P. RATNASINGAM,² R. VANON,¹ P. V. F. EDELMANN,³ AND T. M. ROGERS^{1,4}

¹*Newcastle University*

Newcastle Upon Tyne, United Kingdom

²*Nicolaus Copernicus Astronomical Center*

Polish Academy of Sciences, Poland

³*Los Alamos National Laboratory*

Los Alamos, United States

⁴*Planetary Science Institute, Tucson, AZ, USA*

(Received July 29, 2022; Revised October 5, 2022; Accepted November 5, 2022)

Submitted to ApJ

ABSTRACT

Internal gravity waves (IGWs) can cause mixing in the radiative interiors of stars. We study this mixing by introducing tracer particles into two-dimensional (2D) hydrodynamic simulations. Following the work of [Rogers & McElwaine \(2017\)](#), we extend our study to different masses ($3 M_{\odot}$, $7 M_{\odot}$ and $20 M_{\odot}$) and ages (ZAMS, midMS and TAMS). The diffusion profiles of these models are influenced by various parameters such as the Brunt-Väisälä frequency, density, thermal damping, the geometric effect and the frequencies of waves contributing to these mixing profiles. We find that the mixing profile changes dramatically across age. In younger stars, we noted that the diffusion coefficient increases towards the surface, whereas in older stars the initial increase in the diffusion profile is followed by a decreasing trend. We also find that mixing is stronger in more massive stars. Hence, future stellar evolution models should include this variation. In order to aid the inclusion of this mixing in one-dimensional (1D) stellar evolution models, we determine the dominant waves contributing to these mixing profiles and present a prescription that can be included in 1D models.

1. INTRODUCTION

Chemical mixing plays a major role in stellar evolution. It can transport the chemical elements generated in the nuclear burning region to the surface, creating observed abundance variations. In massive stars, it influences the lifetime of the star by bringing fresh fuel into the burning region leading to a more massive Helium core. Standard stellar evolution theory considers few transport mechanisms or instabilities in the stable radiative zone and yet, very successful in explaining many of the observed properties of stars, such as the mass-luminosity relation, the existence of the main sequence and the evolution towards the giant branch ([Zahn 1994](#)).

However, a series of observed anomalies suggested the need to consider additional mixing processes near the convective-radiative boundary and in the radiation zone; some amongst them are the N/C and $^{13}\text{C}/^{12}\text{C}$ enrichment in low mass stars on the upper red giant branch ([Charbonnel 1994](#)), N abundances in B stars ([Gies & Lambert 1992](#)), He abundances in O and B stars near

the main sequence ([Liubimkov 1975, 1977; Lyubimkov 1989](#)), He discrepancy in O type stars ([Herrero et al. 1992](#)), He and N enrichments in OB supergiants ([Walborn 1976](#)), Li abundances in population II low mass giants ([Pilachowski et al. 1993](#)), and C, N, O abundances in globular cluster giants ([Kraft 1994](#)). Some of the additional physical processes that plausibly cause mixing in these regions are convective overshoot at the convective - radiative boundary ([Zahn 1991; Herwig 2000](#)), rotation ([Zahn 1992; Maeder & Zahn 1998; Maeder & Meynet 2000; Heger et al. 2000](#)), shear induced turbulence ([Zahn 1992; Talon & Zahn 1997; Maeder 2003; Mathis et al. 2004, 2018; Kulenthirarajah & Garaud 2018; Park et al. 2020](#)) internal gravity waves (IGWs) ([Press 1981; Garcia Lopez & Spruit 1991; Charbonnel & Talon 2007; Rogers & McElwaine 2017, hereafter RM17](#)) and magnetic fields ([Maeder & Meynet 2005; Heger et al. 2005](#)). Over the years stellar evolution models focused on the inclusion of these additional mechanisms and using the different prescriptions given by [Kippenhahn et al. \(1970\)](#), [Endal & Sofia \(1976\)](#),

Zahn (1992), Maeder & Zahn (1998), Herwig (2000), Spruit (2002), etc. these mechanisms are implemented in stellar evolution models such as MESA, FRANEC, STERN, GENEC, STAREVOL, etc (Paxton et al. 2011, 2013, 2015, 2018, 2019; Siess et al. 2000; Eggenberger et al. 2008; Brott et al. 2011; Chieffi & Limongi 2013). These models were successful in explaining many observed anomalies such as the observed Nitrogen enhancement in the early universe (Hirschi 2007), surface enrichment of He and C in Main sequence stars (Heger & Langer 2000), blue side of the Li dip and low Li abundances in subgiants (Palacios et al. 2003).

Mixing by convective overshooting is one of the oldest problems studied in stellar astrophysics. Overshooting occurs when the motion of matter extends beyond the boundary determined by either the Ledoux or Schwarzschild stability criteria and continues into the stable layer. Convective matter overshoots outward from the convective core to the radiative envelope in stars more massive than the sun, while for solar-type stars ($0.85 \leq M/M_{\odot} \leq 1.2$) the process is inward, from the convective envelope, leading it to also be called "undershooting"; in either case, the phenomenon can play an important role in stellar evolution. Studies by Alongi et al. (1991) showed that convective undershooting modifies the chemical abundance and also explains the bump in the luminosity function of RGB stars in globular clusters. Convective core overshooting extends the lifetime of core H burning by increasing the availability of fuel within the core, lead to a more massive He core and enhancing the luminosity in the later evolutionary track (Maeder 1976; Schröder et al. 1997).

With the recent advancements in asteroseismology, it was found that the distinct signatures in the period spacings of gravity mode spectra can provide information on the extent to which chemical elements are mixed and the nature of mixing in the transition layer between a convective and radiative zone and in the radiative interiors (Monteiro et al. 2000; Noels et al. 2010; Christensen-Dalsgaard et al. 2011; Pedersen et al. 2018; Deheuvels 2020). Asteroseismic studies also reveal a more massive core than expected by the standard stellar evolution theory suggesting the need of extra mixing in the earlier evolutionary stages (Charpinet et al. 2011; Giammichele et al. 2018). Calibration of mixing profiles based on asteroseismic modelling provides an important input for the improvement of stellar evolution models (Pedersen et al. 2021).

Rotation strongly influences stellar evolution and is considered to be a major ingredient in stellar models and may account for the observed abundance anomalies in massive stars. Eddington (1925) proposed that

meridional circulation can induce mixing in stellar interiors and later studies have indicated that this circulation could explain the C to N ratio in many early type stars (Paczynski 1973). Internal mixing by rotation could explain the Li and Be abundances in low mass stars (Pinsonneault et al. 1989), N/C enhancement seen in OB stars (Lyubimkov 1996), the overabundance of He in O stars (Herrero et al. 1992), Li abundances in evolved stars (Canto Martins et al. 2011) and the surface enrichment of O7-8 giants (Martins et al. 2017). More mixing is contributed by differential rotation that generates turbulent motions in stellar interiors, which give rise to various rotationally induced instabilities like Goldreich-Schubert-Fricke Instability (Goldreich & Schubert 1967), ABCD-instability (Spruit et al. 1983) and shear instabilities (Zahn 1992; Brüggen & Hillebrandt 2001; Prat & Lignières 2013; Garaud 2020; Chang & Garaud 2021; Park et al. 2021; Prat & Mathis 2021). These instabilities play a major role in mixing the CNO materials close to the surface in subgiant and giant branch models (Pinsonneault et al. 1989). Although models that included rotation could explain many of the observed anomalies, they failed to account for some of the observed features like the abundance anomalies in red giants (Palacios et al. 2006), the flat solar rotational profile measured by helioseismology (Brown et al. 1989; Matias & Zahn 1997) and the nitrogen abundance in massive stars (Brott et al. 2011; Aerts et al. 2014). Models including rotational induced transport mechanisms such as the meridional circulation and shear instabilities predicted a rapidly rotating stellar core in sub-giants (Ceillier et al. 2013), red giants (Eggenberger et al. 2012; Marques et al. 2013; Cantiello et al. 2014) and γ Doradus main-sequence intermediate-mass stars (Ouazzani et al. 2019) contradicting the core rotation revealed by asteroseismic observations. This also suggests the need to consider additional transport mechanisms in the stellar interiors.

Apart from rotation, magnetism could also be a source of extra mixing in stars. Maeder & Meynet (2005) studied a magnetic model with the inclusion of meridional circulation and found a significant enrichment in N and He compared to rotating models without an internal magnetic field. Later studies argued that it is likely for magnetic buoyancy to transport materials in AGB and RGB stars (Busso et al. 2007; Nordhaus et al. 2008; Vescovi et al. 2020).

Recently thermohaline mixing, which occurs because of the molecular weight inversion, was proposed to influence the surface abundances in low mass red giants (Charbonnel, C. & Zahn, J.-P. 2007; Eggleton et al. 2006). It could explain the ^3He , Li, C and N abun-

dance in the low mass stars above the RGB bump and the high Li abundances in low mass AGB stars. (Charbonnel & Lagarde 2010; Stancliffe 2010; Lagarde et al. 2011). Cantiello & Langer (2010) investigated the role of this mixing along with rotational mixing and internal gravity fields in low-mass stars. They confirmed that this mixing could explain the decrease in He abundance in RGB stars with an initial mass less than $1.5M_{\odot}$.

Internal Gravity Waves (IGWs) can also cause extra mixing in the radiative interiors (Press 1981; Montalban 1994; Montalban & Schatzman 1996; Montalbán & Schatzman 1993; Rogers & McElwaine 2017). IGWs are naturally occurring waves that propagate in stably stratified fluids with gravity as the restoring force. In stars, IGWs are generated at the convective - radiative interface either by bulk excitation through Reynolds stress (Kumar et al. 1999; Belkacem et al. 2009; Samadi et al. 2010; Lecoanet & Quataert 2013) or by direct excitation through plumes (Hurlburt et al. 1986; Montalbán & Schatzman 2000; Pinçon et al. 2016). Press (1981) considered that the turbulent motion in the convective zone is characterised by eddies and studied the turbulent mixing by IGWs in stars with a convective envelope. He proposed that IGWs could explain the solar neutrino discrepancy. Garcia Lopez & Spruit (1991) argued that the turbulence generated by the internal gravity waves propagating in radiative interiors can explain the Li gap in F type stars. Montalban (1994) used plume morphology based on convective penetration (Zahn 1991) to describe the perturbation at the boundary and explained the observed Li abundance in the Sun (Montalban & Schatzman 1996). RM17 studied the mixing by IGWs in massive stars and determined that it can be treated as a diffusive process with the diffusion profile set by the square of the wave amplitude. Theoretical models including rotation and IGWs were successful in providing insight into the surface Li abundance in low mass stars (Talon & Charbonnel 2005; Charbonnel & Talon 2007).

In this paper, we focus on the mixing by IGWs in stars with a convective core and a radiative envelope. We extend the studies of RM17 to obtain the mixing profiles for stars of higher masses and different ages. We achieve this by running 2D simulations using a background reference model obtained from Modules for Experiments in Stellar Astrophysics (MESA) (Paxton et al. 2011, 2013, 2015, 2018, 2019). We then determine the dominant wave contributing to these mixing profiles using the prescription given by RM17. Section 2 explains the 2D simulations and the tracer particle simulations done to obtain the mixing profiles. Section 3 introduces our results on the mixing profiles for the different models

including a brief description of the theoretical calculations used in this work and Section 4 summarises our findings.

2. BACKGROUND AND NUMERICAL METHODS

2.1. Two-Dimensional Simulation

We generated the stellar models for three masses ($3 M_{\odot}$, $7 M_{\odot}$, $20 M_{\odot}$) at three ages (Zero Age Main Sequence (ZAMS, core hydrogen mass fraction, $X_c = 0.7$), mid-Main Sequence (midMS, $X_c = 0.35$), Terminal Age Main Sequence (TAMS, $X_c=0.01$) from MESA. We set the overshooting parameter to 1.8 and the convective overshoot profile to exponential, implemented the mass loss through Van Loon stellar wind scheme and considered zero rotation in our models. The inlists used to generate the models are given in Appendix A and also available in zenodo.

We calculated the Brunt-Väisälä frequency, N based on the work of Rogers et al. (2013),

$$N^2 = \frac{\bar{g}}{\bar{T}} \left(\frac{d\bar{T}}{d\bar{r}} - (\gamma - 1)\bar{T}h_{\rho} \right). \quad (1)$$

where \bar{g} , \bar{T} , γ and h_{ρ} are the reference state gravity, temperature, the adiabatic index and the negative inverse density scale height. The location of the convective-radiative interface is determined by the sign of the Brunt-Väisälä frequency where

$$N^2 > 0 \quad (2)$$

is the radiation zone and

$$N^2 < 0 \quad (3)$$

is the convection zone. The background density and the Brunt-Väisälä frequency profiles of all the models considered in this work are shown in Fig. 1.

To study IGWs in stellar interiors, we solved the Navier-Stokes equations in the anelastic approximations using 2D hydrodynamic simulations considering an equatorial slice of the star with stress-free, isothermal and impermeable boundary conditions (Rogers et al. 2013). The numerical model followed in this work is similar to that of Rogers et al. (2013) and the 2 D simulations are run by R.P Ratnasingam (more details on the simulations can be found in Ratnasingam (2020), Ratnasingam et al. 2022 in prep).

Fig. 2 shows the time snapshots of vorticity for all the models considered in this work.

The thermal diffusivity (κ) and viscosity (ν) are set to constant values shown in Table. 1. Our objective was to attain the highest Reynolds number, Re,

$$\text{Re} = \frac{v_{rms}L}{\nu}. \quad (4)$$

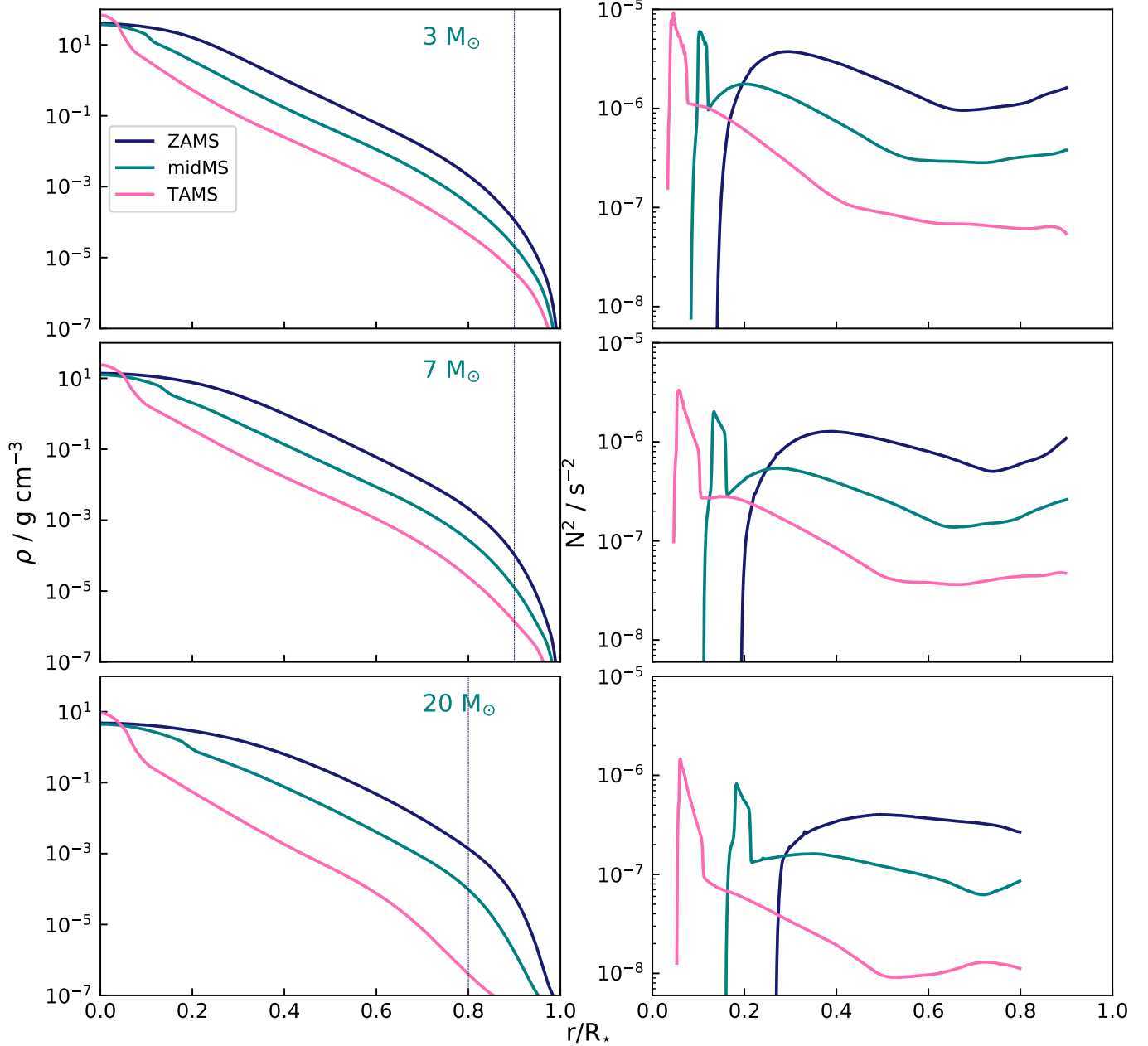


Figure 1. Density (left panel) and Brunt-Väisälä frequency (right panel) and as a function of fractional radius for $3 M_\odot$ (top panel), $7 M_\odot$ (middle panel), $20 M_\odot$ (bottom panel) at ZAMS, midMS and TAMS. The vertical dashed line in the density plot indicates the cut off radii of the simulation domain.

for each model studied. Here v_{rms} is the root mean squared velocity averaged over the convection zone and L is the characteristic length scale (the radial extent of the convection zone in this case). We also aimed to attain convective velocity ratios for different masses from our simulations which are comparable to those predicted by the mixing-length theory (MLT) velocities in MESA for any given age. (We chose to compare across masses as the uncertainties in the MLT velocities in MESA are larger across ages). We therefore chose the values such

that the above are satisfied whilst maintaining numerical stability. The simulation is run for an average time of approximately, 2.7×10^7 s for the models studied.

The simulation domain extends up to 90% of the total stellar radius for all the $3 M_\odot$ and $7 M_\odot$ models and up to 80% of the total stellar radius for all the $20 M_\odot$ models. The cut-off radius is determined such that the density does not vary more than ~ 6 orders of magnitude as we move from the inner to the outer boundary to maintain numerical stability. As evident from Fig. 1,

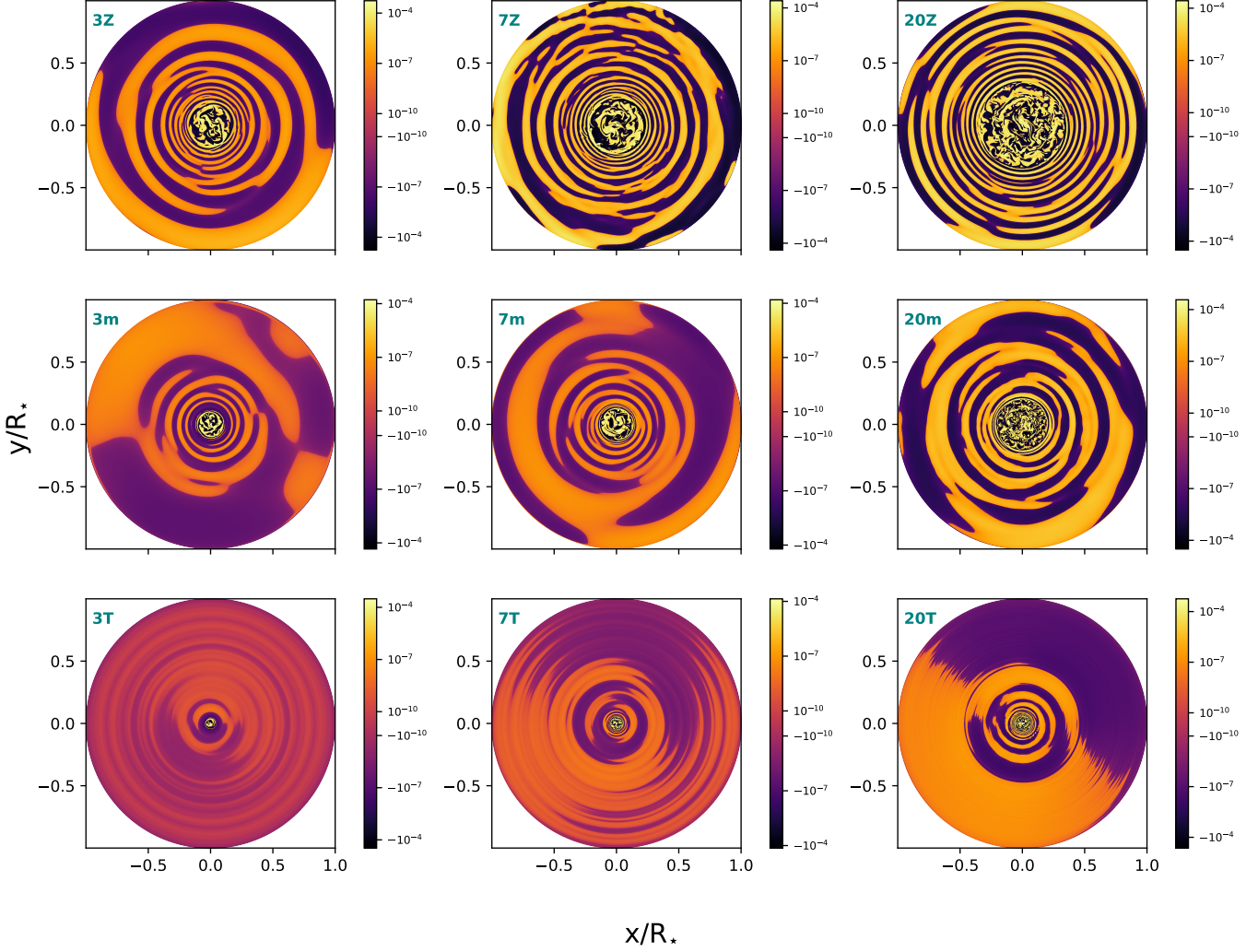


Figure 2. Vorticity for $3 M_{\odot}$ (left), $7 M_{\odot}$ (middle) and $20 M_{\odot}$ (right) at ZAMS (top panel), mid-MS (middle panel) and TAMS (bottom panel).

Model	$\kappa, \nu / 10^{12} \text{ cm}^2 \text{ s}^{-1}$	Convective turnover times
$3M_{\odot}$ ZAMS	5	123
$3M_{\odot}$ midMS	5	91
$3M_{\odot}$ TAMS	5	105
$7M_{\odot}$ ZAMS	5	62
$7M_{\odot}$ midMS	5	70
$7M_{\odot}$ TAMS	2.5	67
$20M_{\odot}$ ZAMS	8	40
$20M_{\odot}$ midMS	8	58
$20M_{\odot}$ TAMS	5	52

Table 1. Thermal and viscous diffusivities of the different models used in our simulation along with the total time interval in terms of convective turnover times considered for our analysis.

this is satisfied only until $0.9R_{\star}$ for $3 M_{\odot}$ and $7 M_{\odot}$ models and up to $0.8R_{\star}$ for $20 M_{\odot}$ models. We therefore chose these respective domains for our simulations. For our analysis, we chose the velocity data from a time, $4 \times 10^6 \text{ s}$ for all the $3 M_{\odot}$ and $7 M_{\odot}$ models and from $6 \times 10^6 \text{ s}$ ¹ for all the $20 M_{\odot}$ models. The total time window considered is given in terms of convective turnover times in Table. 1. We then used this velocity data which is saved at a regular time interval to study the mixing by IGWs in stellar interiors.

2.2. Tracer particle simulation

¹ We found that the IGWs show a steady state evolution from this value in our 2D hydrodynamic simulation. Steady-state evolution refers to a state when the amplitudes of the IGWs remain constant over time.

To measure the mixing by IGWs in stellar interiors, we introduce \mathcal{N} tracer particles into our simulation and track them over a time T . This procedure is carried out in post-processing and we use the relations given by RM17 to calculate the diffusion coefficient $D(r, \tau)$ at radius r , for a given time difference, τ .

$$D(r, \tau) = \frac{Q(r, \tau)}{2\tau n(r, \tau)} - \frac{P(r, \tau)^2}{2\tau n(r, \tau)^2}. \quad (5)$$

where $n(r, \tau)$, is the number of sub-trajectories starting at r with a duration of τ , $P(r, \tau)$ is the sum of the lengths of the sub-trajectories and $Q(r, \tau)$ is the sum of the square of these sub-trajectories. More details on the calculation of n , P , Q and $D(r, \tau)$ can be found in RM17.

We then plotted the diffusion coefficients calculated using the above equation as a function of radius. We varied different parameters such as the number of particles, radial grid size and velocity timesteps in our simulation to check for numerical convergence and obtained the diffusion coefficient for each set of parameters. Fig. 3 shows the radial diffusion profiles with (a) different velocity time steps Δt (b) different radial grid sizes and (c) different number of particles \mathcal{N} , for a $7 M_{\odot}$ ZAMS model. In each case, the profiles appear converged with respect to the variables changed. We extended the same treatment to all the other stellar models and found the radial diffusion profile to be already converged for a time resolution of 1000s, radial resolution of 500 and particle resolution of 10000. This is consistent with RM17 who found the mixing profile robust to parameter changes. Henceforth, we choose these values for all our further analysis and obtain the radial diffusion profile at a time difference ² of 1.3×10^7 s for all the three masses.

3. RESULTS

We found the general trend of the diffusion profile to be increasing from the convective - radiative interface towards the surface as seen in Fig. 3 consistent with the results of RM17. However as the star ages, its properties such as the density and the Brunt-Väisälä frequency change is evident from Fig. 1. These changes also affect the diffusion coefficient. Here, we investigated the dependence of age and mass on the radial diffusion profiles.

3.1. Age dependencies

² The smaller τ has contributions from more time steps compared to a larger value of τ . As an example, consider $T=100$ with time step = 1. Then, for $\tau = 5$, it has contributions from 5 - 0, 6 - 1, 7 - 2 and so on, whereas $\tau = 97$ can result only from 100 - 3, 99 - 2 and 98 - 1.

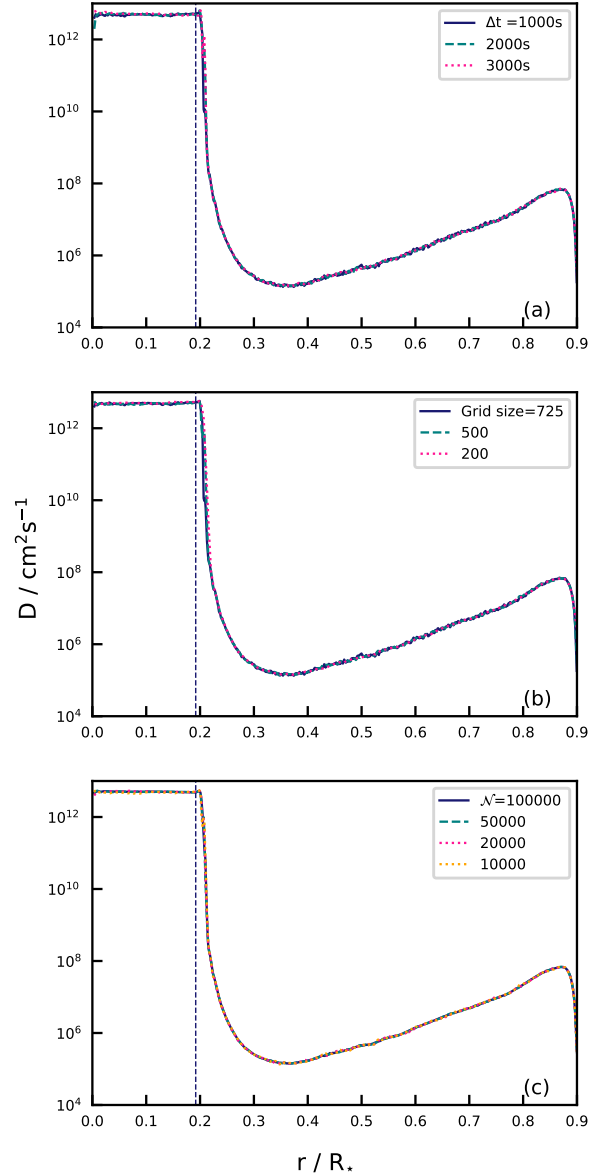


Figure 3. Radial diffusion profiles for varying parameters (a) Velocity time step (Δt) (b) Radial grid size (c) Number of particles (\mathcal{N}) for $7 M_{\odot}$ ZAMS model at $\tau = 1.2 \times 10^6$ s. The blue vertical dashed line indicates the convective - radiative interface

Fig. 4 shows the radial diffusion profiles at ZAMS (Blue), midMS (green) and TAMS (pink) for $3 M_{\odot}$, $7 M_{\odot}$ and $20 M_{\odot}$ models. In general, we find that the mixing profile varies significantly across the ages for all the masses studied. The amplitude of the diffusion profile depends on several factors such as the wave driving, density stratification, thermal diffusivity, the Brunt-Väisälä frequency and the geometric effect. Among these, density stratification and thermal diffusivity dominate in both ZAMS and midMS stars, hence the diffusion coef-

ficient increases with stellar radius following the density stratification modulated by the thermal diffusion.

However, the mixing profile at TAMS shows an increasing trend from the convective - radiative interface followed by a *decreasing* trend towards the surface which is considerably different from that of the younger stars. To understand this behaviour, we looked at the following second - order differential equation for wave propagation,

$$0 = \frac{\partial^2 \alpha}{\partial r^2} + \left[\frac{N^2}{\omega^2} - 1 \right] \frac{m^2}{r^2} \alpha + \frac{1}{2} \left[\frac{\partial h_\rho}{\partial r} - h_\rho^2 + \frac{h_\rho}{r} \right] \alpha + \frac{1}{4r^2} \alpha \quad (6)$$

which is obtained by reducing the linearised 2D hydrodynamic equations considering no thermal or viscous diffusion with $\alpha = v_r \bar{\rho}^{\frac{1}{2}} r^{\frac{3}{2}}$ and m is the 2D Fourier basis wavenumber. In younger stars, the first two terms dominate over most of their radii. However, in older stars, the density term,

$$\frac{1}{2} \left[\frac{\partial h_\rho}{\partial r} - h_\rho^2 + \frac{h_\rho}{r} \right], \quad (7)$$

becomes dominant at larger radii.

We define turning point as the radius at which the ratio of the oscillatory term,

$$\left[\frac{N^2}{\omega^2} - 1 \right] \frac{m^2}{r^2}. \quad (8)$$

to that of the density term $\left(\frac{1}{2} \left[\frac{\partial h_\rho}{\partial r} - h_\rho^2 + \frac{h_\rho}{r} \right] \right)$ is equal to 1 (Ratnasingam et al. 2020) and it is located at a lower fraction of the total radius in older stars. Waves lose their wave like behaviour when this ratio is less than one and as a result they experience extra damping. This leads to waves becoming evanescent towards the surface and leads to the diffusion profile we see in Fig. 4. The shaded region in the plot indicates the location of turning points for the TAMS models using the range of frequencies ($4 - 14 \mu\text{Hz}$) determined in Section 3.4.

Another factor contributing to the diffusion profiles of TAMS models is the Brunt-Väisälä frequency spike near the convective-radiative interface left behind by a steep composition gradient as the star evolves from ZAMS (Fig. 1). This peak damps many waves near the convective - radiative interface and traps the higher frequencies resulting in fewer waves contributing to mixing, thereby leading to a decrease in the diffusion coefficient. In general, TAMS models have a significantly reduced diffusion coefficient than ZAMS and midMS models.

3.2. Mass dependencies

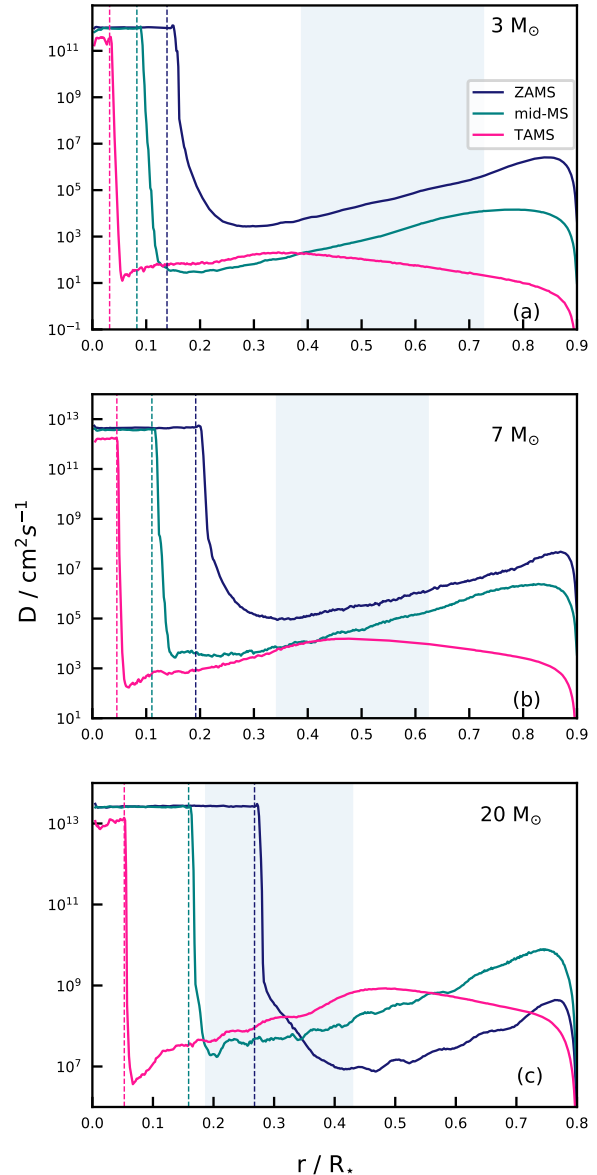


Figure 4. Diffusion coefficient as a function of fractional radius at ZAMS, mid-MS and TAMS for (a) $3 M_\odot$, (b) $7 M_\odot$ and (c) $20 M_\odot$ models. The vertical dashed line represents the convective-radiative interface for each models. The shaded region indicates the location of turning points of the TAMS model for the range of frequencies $4 - 14 \mu\text{Hz}$.

Fig. 5 shows the diffusion profiles as a function of radius for $3 M_\odot$ (green), $7 M_\odot$ (pink) and $20 M_\odot$ (blue) at different ages. As evident from the figure, the mixing is stronger in massive stars, and this can be accounted for by the stronger convective driving in massive stars. Another factor contributing to the increase in the diffusion coefficient with mass is the Brunt-Väisälä frequency. As noted from Fig. 1, the Brunt-Väisälä frequency decreases with increasing mass. This leads to lower damp-

ing of waves in stars with higher mass and hence results in stronger mixing than lower mass stars.

3.3. Parameterization of the Diffusion Coefficient

RM17 determined the diffusion profile in the radiation zone to be set by the square of the wave amplitude given by

$$D = Av_{wave}^2(\omega, l, r), \quad (9)$$

where the coefficient A was speculated to depend on the diffusivities, rotation and dimensionality and was found to be ~ 1 s by RM17.

To test this theory against the new data, we calculated the wave amplitudes using the linear theory given by Ratnasingam et al. (2018) where they solved the anelastic, linearised hydrodynamic equations within the WKB approximation without considering the rotational, thermal and viscous effects. The equation is given by

$$v_{wave}(\omega, l, r) = v_0(\omega, l, r) \left(\frac{\rho}{\rho_0} \right)^{\frac{1}{2}} \left(\frac{r}{r_0} \right)^{-1} \left(\frac{N^2 - \omega^2}{N_0^2 - \omega^2} \right)^{-\frac{1}{4}} e^{-\frac{\mathcal{T}}{2}}, \quad (10)$$

where ρ_0 , r_0 and N_0 are the density, radius and the Brunt-Väisälä Frequency at the initial reference point. $v_0(\omega, l, r)$ is the initial wave amplitude for a given frequency and wavenumber. The radial velocity is related to the tangential velocity by the following relation,

$$\frac{v_\theta}{v_r} = \left(\frac{N^2}{\omega^2} - 1 \right)^{\frac{1}{2}}, \quad (11)$$

The above can be approximated to $\frac{N}{\omega}$ for frequencies much smaller than the Brunt-Väisälä Frequency. We therefore assume the wave amplitude to be equal to the root mean squared velocity at the reference point averaged over the time window considered (see Section 2.1) multiplied by a factor of $\frac{\omega}{N}$ to obtain the theoretical radial diffusion profiles. The term $\exp(-\frac{\mathcal{T}}{2})$ in the above equation is the attenuation factor multiplied to the wave amplitude as the radiative damping is considered within the quasi adiabatic limit (Zahn et al. 1997). The damping coefficient \mathcal{T} according to Kumar et al. (1999) is given as:

$$\mathcal{T}(\omega, l, r) = \int_{r_0}^r \frac{16\sigma T^3}{3\rho^2 \kappa c_p} \left(\frac{(l(l+1))^{\frac{3}{2}} N^3}{r^3 \omega^4} \right) \left(1 - \frac{\omega^2}{N^2} \right) dr. \quad (12)$$

where σ , T , c_p , κ and l are the Stefan-Boltzmann constant, temperature, specific heat capacity at constant pressure, opacity and wavenumber. RM17 studied a 3

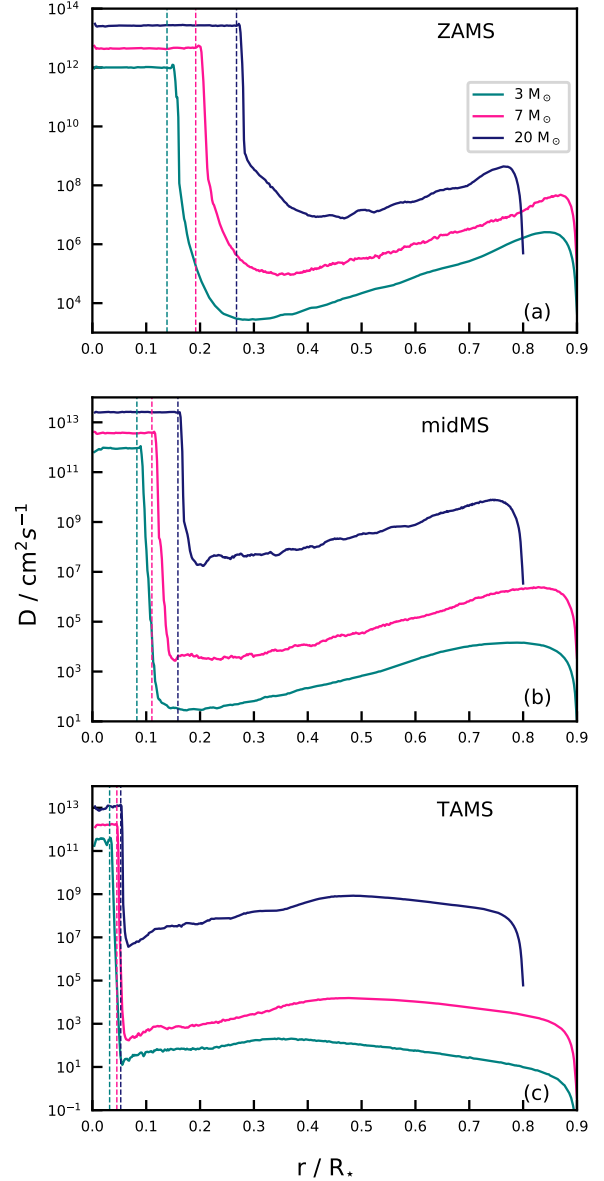


Figure 5. The diffusion coefficient as a function of fractional radius for $3 M_\odot$, $7 M_\odot$ and $20 M_\odot$ at (a) Zero Age Main sequence (b) mid - Main sequence and (c) Terminal Age Main Sequence. The vertical dashed line represents the convective-radiative interface for each models.

M_\odot midMS model considering up to 70 % of the total stellar radius without taking into account the effect of the Brunt-Väisälä Frequency on the wave amplitude. We extend their analysis to stellar models presented in this work by considering a modified relation to calculate the wave amplitude (Eqn. 10) based on the linear theory given by Ratnasingam et al. (2018).

3.4. Determining the dominant frequencies contributing to the mixing profiles

In order to incorporate this mixing into 1D stellar evolution codes, we need to determine the dominant waves contributing to the mixing profiles, we launched waves from a radius outside the convective radiative interface and calculated the theoretical diffusion coefficient using Eqns. 9-12 for a set of frequencies (1 – 40 μ Hz) and wavenumbers (1-10) for each stellar model. The initial reference points where the waves are launched are highly influenced by the overshooting motions. We therefore initially determined the overshooting depth for each model by fitting the following Gaussian function to the mixing profile near the convective radiative interface,

$$D = D_0 \exp \left[\frac{(x - cr + f_0 H_p)^2}{2(f_1 H_p)^2} \right] \quad (13)$$

where D_0 is the amplitude, cr is the radius of the convection zone, H_p is the pressure scale height, f_0 and f_1 are the overshooting parameters. We measured the overshooting depth as the radius up to which we could get a good fit of the Gaussian profile. Fig. 6 shows the Gaussian fit along with the mixing profile near the convective radiative interface for a 7 M_\odot ZAMS model as an example. Here, we obtained the mixing profile (blue) near the convective radiative interface from the simulation and then fitted this profile with the Gaussian function (pink) given by Eqn. 13. The overshooting depth determined is indicated by the pink vertical dashed line. We repeated this procedure for all the models and the overshooting depth for the different models found are given in Table 2. We then launched the waves at a radius equal to 1.3³ times the overshooting depth in all the models studied. More details on the overshooting profiles along with the comparison of the overshooting depth determined from the theory and simulation will be discussed in an upcoming paper.

In order to implement a prescription for wave mixing into a 1D code, it would be helpful to narrow down the range of frequencies and wavenumbers contributing to the mixing profile. We therefore compared the theoretical profiles calculated using Eqns. 9-12 at different frequencies and wavenumbers with our simulation diffusion profiles for all the models to determine if a simpler prescription, with limited waves, could be found. We observed that the waves with higher wavenumbers provide a smaller contribution towards the diffusion coefficient since they experience higher thermal damping as expected from Eqn. 12 and therefore, we discard

³ We considered various initial reference points beyond the overshoot depth to launch the waves and found that at this value, the theoretical profiles showed a reasonable agreement with that of the simulation profiles for all the models studied.

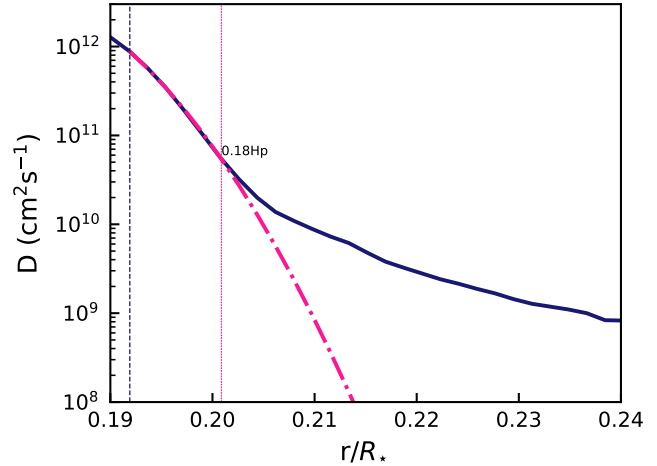


Figure 6. Mixing profile near the convective radiative interface from the simulation (blue) and the Gaussian fit (pink line) with the overshooting depth ($0.18H_p$) indicated by the pink vertical dashed line for a 7 M_\odot ZAMS model. The convective radiative interface is given by the vertical blue dashed line.

their contributions and consider only $l = 1$ waves in our further calculations. We show the theoretical diffusion profiles corresponding to the dominant frequencies that provide the best fit to the profiles from the simulations in Fig. 7. The figure also shows the theoretical profiles at different frequencies as an example (dotted profiles in Fig. 7). In general, the mixing profiles obtained from the linear theory corresponding to the dominant frequencies are in good agreement with the simulations diffusion profiles for all ZAMS (Fig. 7 (a), (b), (c)) and midMS (Fig. 7 (d), (e), (f)) models.

We found the dominant frequencies for the different models studied to be in the range of 4 – 9 μ Hz at wavenumber $l = 1$; with the lower frequencies being dominant for massive stars. This can be attributed to the thermal damping given by Eqn. 12. Even though the lower frequencies are generated with larger amplitude near the convective-radiative interface, these waves are highly affected by thermal damping. As noted from Fig. 1, the average Brunt-Väisälä frequency decreases with mass, causing the effect of damping to be less dominant in massive stars and thereby resulting in lower dominant frequencies. We also noted that the waves experience extra damping near the convective radiative interface in all the midMS models because of the Brunt-Väisälä frequency peak as noted from Fig. 1. The theoretical profiles do not match the numerical simulations well at the surface, nor interface. At the surface, this is because the radial velocity is forced to zero in our hydrodynamic simulations, causing the amplitude of our numerical profile to drop near the surface which is not

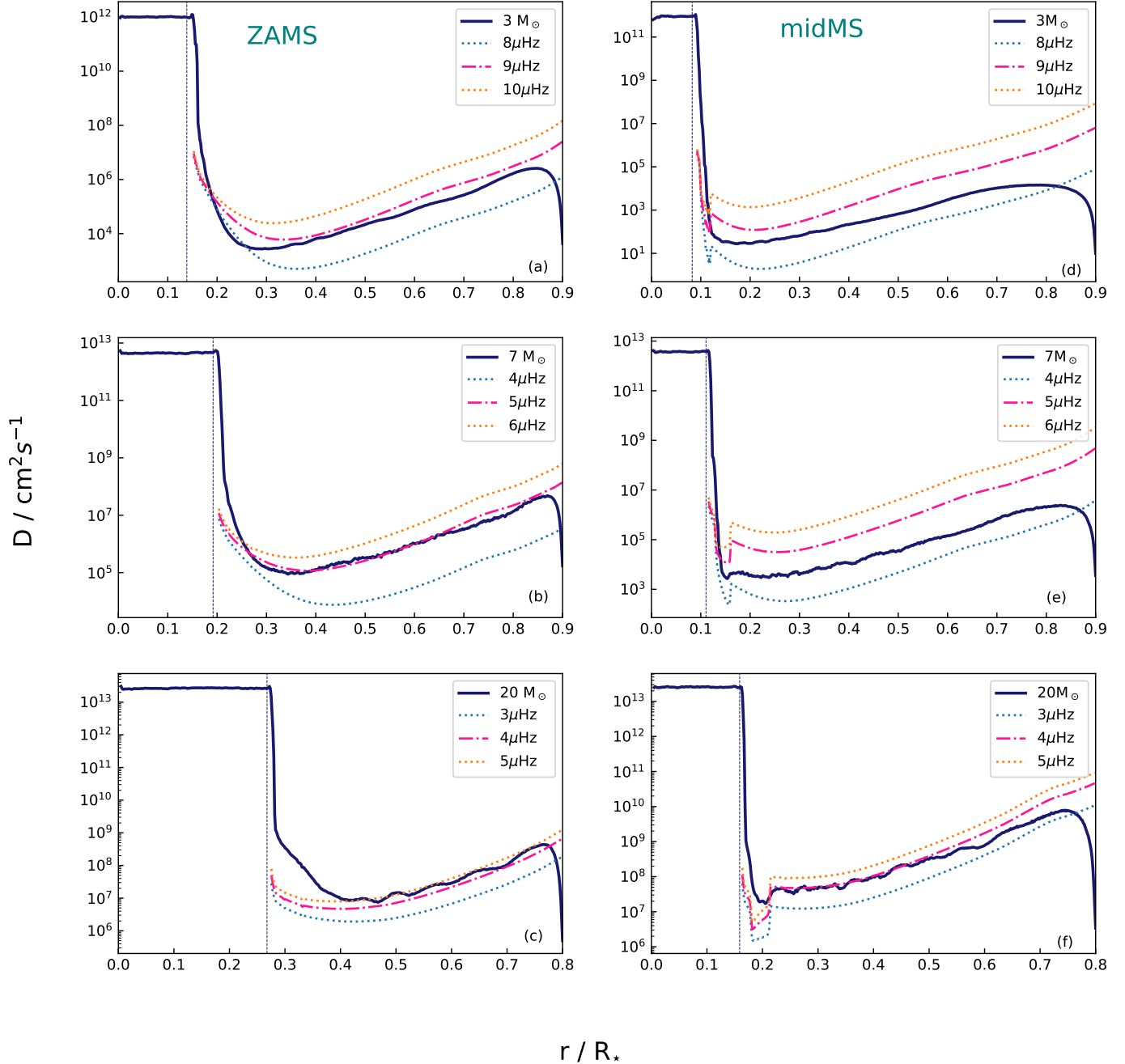


Figure 7. Diffusion coefficient as a function of fractional radius for 3, 7 and 20 M_⊙ at ZAMS (left panel) and midMS models (right panel) from the simulation (blue line) and from the linear theory with waves launched at $1.3H_p$ for the dominant frequencies (pink line). The dotted profiles shows the theoretical profiles at different frequencies.

necessarily physical. At the interface, convective overshooting means the region is not totally dominated by waves (Rogers et al. 2006). In our models, the deviation of the theoretical diffusion profile from that of the simulation near the interface, particularly in the case of ZAMS can be explained by these overshooting motions, as they influence the determination of the initial reference point at which the waves are to be launched.

We followed the same procedure to calculate the theoretical diffusion profiles for the TAMS models. We found that none of the theoretical profiles could explain the profile from the numerical simulation accurately. Fig. 8 shows the best match that we could get from our analysis for the different TAMS models (pink dot-dashed profiles). The pink vertical dashed line represents the turning point for the frequencies shown. We can clearly see that the profiles start to diverge as they approach the

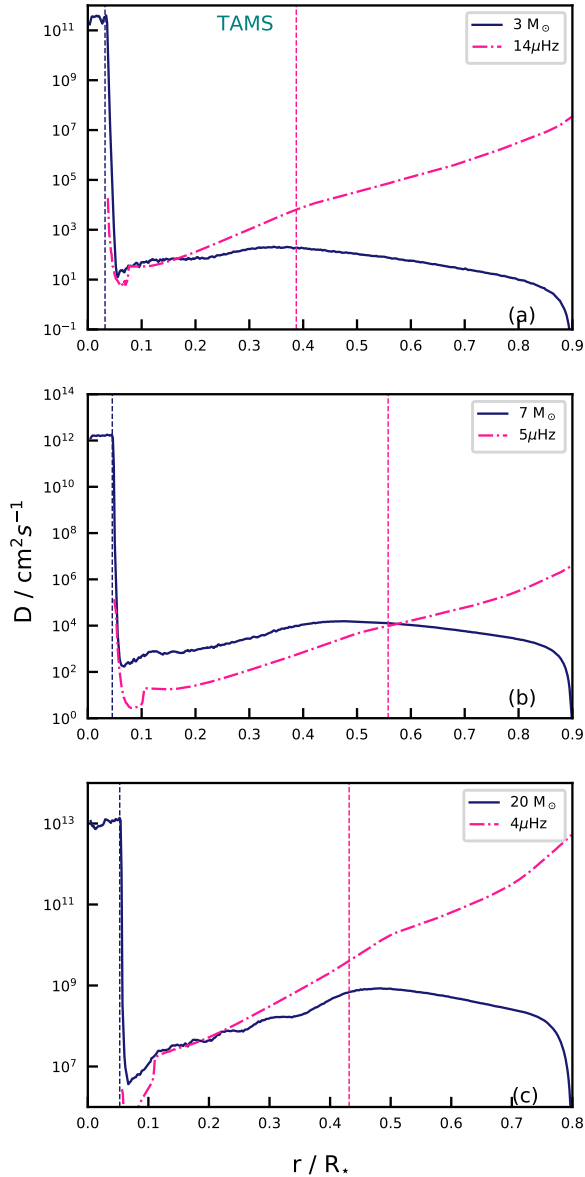


Figure 8. Diffusion coefficient as a function of fractional radius for 3, 7 and 20 M_{\odot} at TAMS from the simulation (blue line) and from the linear theory (pink line). The pink vertical dashed line indicates the turning point corresponding to the frequencies shown.

turning point beyond which the waves become evanescent. As stated previously, the waves lose their wave like behaviour at a lower fraction of the total stellar radius because of the density term in Eqn. 6 being dominant for a major fraction of the radius in older stars. Therefore the WKB approximation applied to the equation for wave propagation (Eqn. 6) is not valid in the TAMS models and hence the theoretical description outlined in RM17 and Section 3.3 is not valid in older stars. More analysis needs to be carried out in the future for a bet-

Model	Overshooting Depth (Units of H_p)
3 M_{\odot} ZAMS	0.22
3 M_{\odot} midMS	0.20
3 M_{\odot} TAMS	0.17
7 M_{\odot} ZAMS	0.18
7 M_{\odot} midMS	0.105
7 M_{\odot} TAMS	0.12
20 M_{\odot} ZAMS	0.14
20 M_{\odot} midMS	0.11
20 M_{\odot} TAMS	0.22

Table 2. The overshooting depths in the units of pressure scale height (H_p) for the different models.

ter understanding of the diffusion profiles of the TAMS models. However, at this stage it appears that a substantially lower diffusion coefficient, which is virtually flat throughout the radiation zone is a decent approximation of wave mixing at late stages of stellar evolution.

We also computed the kinetic energy spectrum, \hat{E}_{kin} ,

$$\hat{E}_{\text{kin}} = \frac{1}{2} \bar{\rho} (\hat{v}_r^2 + \hat{v}_\theta^2) \quad (14)$$

where, \hat{v}_r and \hat{v}_θ are the Fourier transforms of radial and tangential velocities. Fig. 9 shows the frequency distribution of the kinetic energy for $l = 1$ at three different radii where the top panel (a, b, c) presents the spectra at 1.3 times the overshoot depth (radius at which the waves are launched), the middle panel (d, e, f) at $0.3R_*$ and the bottom panel (g, h, i) at $0.6R_*$ for all the models studied. The vertical dashed lines indicate the dominant frequencies shown in Fig. 7 and Fig. 8. We note that the dominant frequencies lie close to where the kinetic energy density peaks, thereby justifying our choice of frequencies. This is more evident from the middle and bottom panels of Fig. 9. We are not concerned with the TAMS models as we have already shown that the linear theory does not explain their mixing profiles accurately.

3.5. Determination of the parameter A

We conducted a number of tests to determine the value of the parameter 'A' from our simulations. We found that the simulation should be run for longer convective turnover times for the correct estimate of this parameter. Regardless of how long the simulations were run, the mixing profiles maintained the same trends discussed in Section 3.1 and 3.2. But, we noted that the amplitudes of the profiles decrease further and converge at higher time differences. This is shown in Fig. 10(a) for the 7 M_{\odot} ZAMS model run for 87 convective turnover times. We see that the amplitude of the mixing profile converges at $\sim \tau = 3 \times 10^7$ s. We then compared this

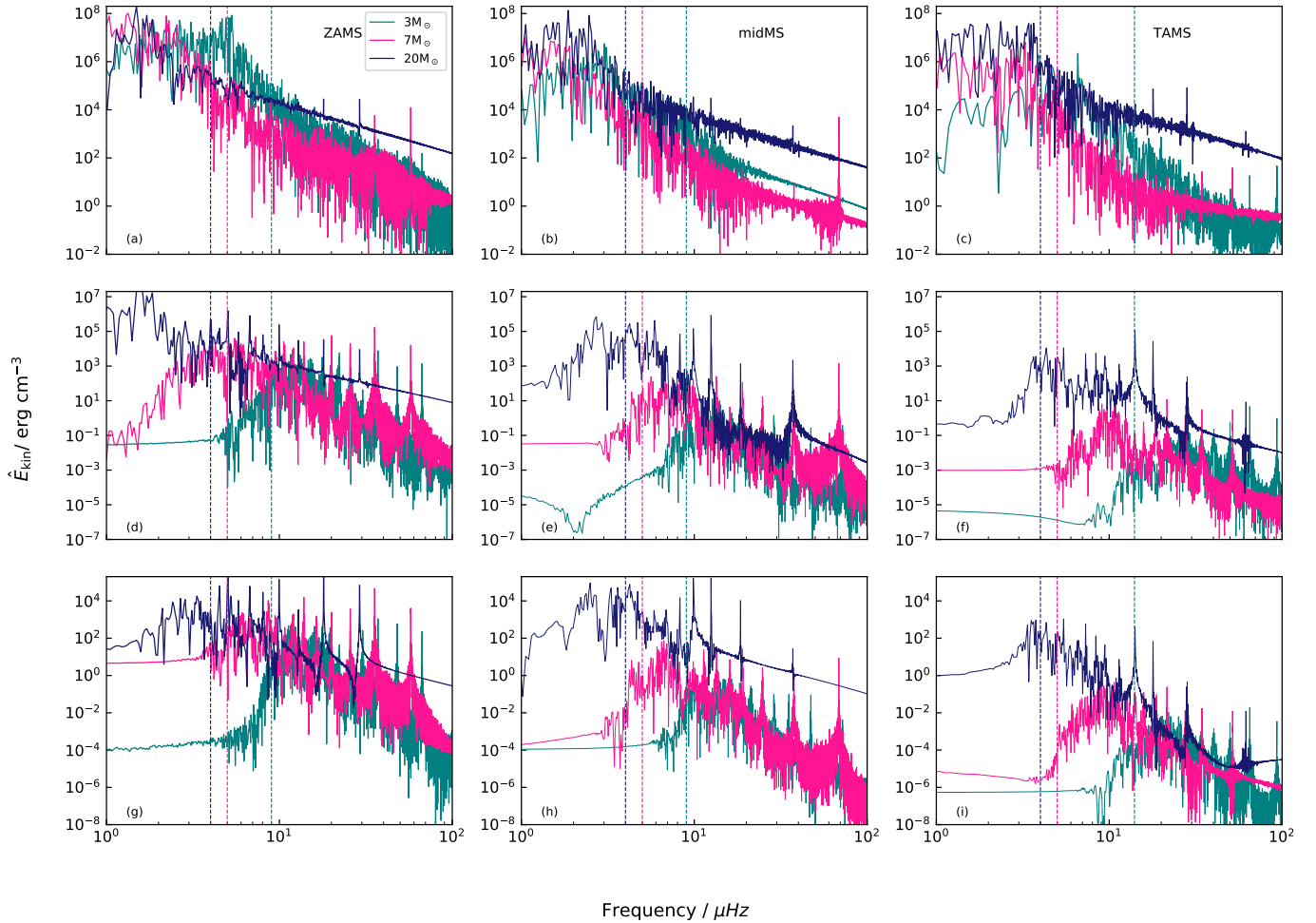


Figure 9. The frequency distribution of the kinetic energy density for $3 M_{\odot}$ (green), $7 M_{\odot}$ (pink) and $20 M_{\odot}$ (blue) at ZAMS (left column), midMS (middle column) and TAMS (right column) in the radiation zone at 1.3 times the overshoot depth (top row), $0.3R_{\star}$ (middle row) $0.6R_{\star}$ (bottom row). The vertical dashed lines indicate the dominant frequencies shown in Fig. 7 and Fig. 8.

profile to the square of wave amplitude (here the amplitude is summed over a range of frequencies ($1 - 40 \mu\text{Hz}$) and wavenumbers ($1-20$)⁴) obtained from the simulation (pink in Fig. 10 (b)). As evident from the figure, both the profiles matches to a good extend, giving us the value of the parameter 'A' ~ 1 . We expect all the models to show similar behaviour once the simulation is run for longer convective turnover times. Our finding is in agreement with that of RM17. A better estimate of this parameter can only be obtained by the comparison of our theoretical prescription with that of the observations.

4. CONCLUSION

⁴ The wave amplitudes were negligible at higher wavenumbers, hence we neglected their contributions in our calculation.

We studied the mixing by IGWs in stars of different masses and ages by introducing tracer particles into our 2D hydrodynamic simulations. Initially, we carried out a convergence test for all our models to check if they agreed with the studies of RM17. We found that all our models attained numerical convergence with respect to the time, particle and radial resolution. We then focused our attention on the diffusion profiles as a function of mass and age.

One of our main conclusions is that the mixing profile varies significantly across age with the mixing stronger in younger stars. The different trend observed in the mixing profiles of TAMS models can be accounted for by the turning point which is located at a lower fraction of the total stellar radius and the Brunt-Väisälä frequency spike in these older stars. We also found that mixing by IGWs is stronger for stars of higher masses. The stronger convective driving in massive stars along

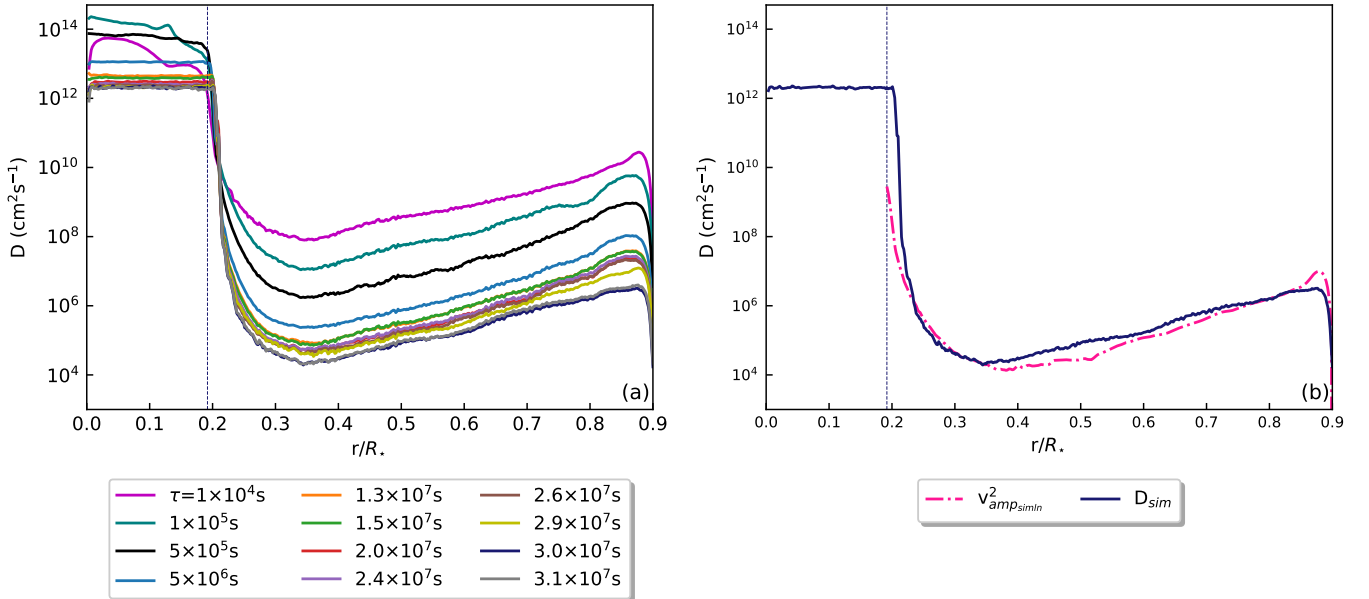


Figure 10. (a) Radial diffusion profile for the $7 M_{\odot}$ ZAMS model at different time differences (τ). (b) The square of the wave amplitude (summed over frequencies ($1 - 40 \mu\text{Hz}$) and wavenumbers (1-20)) from the simulation (pink) along with diffusion profile (blue) at $\tau = 3 \times 10^7 \text{s}$.

with the lower average Brunt-Väisälä frequency result in higher amplitude waves within the radiative zone and therefore, more mixing.

We then tested our simulation results against the prescription given by RM17 for the inclusion of these mixing profiles in one dimensional stellar evolution models. We found that their theory agrees well with the simulation for all ZAMS and midMS models with the dominant waves contributing to these mixing profiles in the range of $4 - 9 \mu\text{Hz}$ for wavenumber $l = 1$. We also found that the dominant frequency decreases with increasing mass, but remains approximately the same across different ages for a given mass as can be noted from Fig. 7. When run for longer time, we find that the amplitude of the mixing profile converges such that $A \sim 1$. It is still unclear what physically sets this parameter. The linear theory however failed to explain the mixing profiles of TAMS models because the waves cannot be described by the WKB approximation. Studies attempting to find a prescription for the TAMS models will be forthcoming.

Future work will focus on determining the effect of rotation on the mixing by IGWs in the radiation zone

by extending our analysis to models of different rotation rates. We aim to find out how rotation influences the turning point in older stars.

5. ACKNOWLEDGEMENTS

We acknowledge support from STFC grant ST/L005549/1 and NASA grant NNX17AB92G. Computing was carried out on Pleiades at NASA Ames, Rocket High Performance Computing service at Newcastle University and DiRAC Data Intensive service at Leicester, operated by the University of Leicester IT Services, which forms part of the STFC DiRAC HPC Facility (www.dirac.ac.uk), funded by BEIS capital funding via STFC capital grants ST/K000373/1 and ST/R002363/1 and STFC DiRAC Operations grant ST/R001014/1. PVFE was supported by the U.S. Department of Energy through the Los Alamos National Laboratory (LANL). LANL is operated by Triad National Security, LLC, for the National Nuclear Security Administration of the U.S. Department of Energy (Contract No. 89233218CNA000001). This paper was assigned a document release number LA-UR-22-27682.

APPENDIX

A. MESA INLIST FILES

The MESA inlists used to generate the models in this work are given below. To keep comparisons consistent, we just changed the mass and the value of X_c

(`xa_central_lower_limit(1)`) in the inlists without changing any other parameters.

The macro and micro physics details are implemented using `inlist_project`:

```

&star_job
! mesa_dir = '$MESA_DIR'
create_pre_main_sequence_model = .false.
show_log_description_at_start = .false.
show_net_species_info = .false.
show_net_reactions_info = .false.
show_eqns_and_vars_names = .false.
!history_columns_file = 'hist.list'
!profile_columns_file = 'prof.list'
report_retries = .false.
report_backups = .false.
initial_zfracs = 6
change_v_flag = .true.
new_v_flag = .true.
change_lnPgas_flag = .true.
new_lnPgas_flag = .true.
change_net = .true.
! switch nuclear reaction network
new_net_name = 'o18_and_ne22.net'
auto_extend_net = .true.
kappa_file_prefix = 'a09'
kappa_lowT_prefix = 'lowT_fa05_a09p'
kappa_blend_logT_upper_bdy = 4.10
kappa_blend_logT_lower_bdy = 4.00
kappa_type2_logT_lower_bdy = 3.8
kappa_CO_prefix = 'a09_co'
/ !end of star_job

&controls
stop_near_zams = .true.
! Initial values
initial_mass = 3.00
initial_z = 2d-2
!initial_y = 0.58
!zams_filename = 'zams_2m2_y58.data'

! controls for output
terminal_interval = 25
write_header_frequency = 5
terminal_show_age_in_years = .true.
photo_interval = 200
photo_digits = 4
!log_directory = 'LOGS'
history_interval = 1
write_profiles_flag = .false.
profile_interval = 100000
priority_profile_interval = 10000
profile_data_suffix = '.prof'
star_history_dbl_format = '(1pes22.6e3, 1x)'
star_history_int_format = '(i22, 1x)'
star_history_txt_format = '(a32, 1x)'
!max_model_number = 1

xa_central_lower_limit_species(1) = 'h1'
xa_central_lower_limit(1) = 0.01d0
! 0.69d0, 0.35d0, 0.01
when_to_stop_rtol = 1d-4
when_to_stop_atol = 1d-4
max_num_profile_models = -1

write_pulse_info_with_profile = .false.
!pulse_info_format = 'FGONG'
add_atmosphere_to_pulse_info = .true.
add_center_point_to_pulse_info = .false.
keep_surface_point_for_pulse_info = .true.

! mixing parameters
use_Ledoux_criterion = .true.
!use_Henyey_MLT = .true.
MLT_option = 'Henyey'
mixing_length_alpha = 1.8
! alpha_semiconvection = 0 ! 0.01
num_cells_for_smooth_gradL_composition_term = 3
radiation_turbulence_coeff = 0

! apply smoothing to abundances in newly
nonconvective regions
smooth_convective_bdy = .true.
max_delta_limit_for_smooth = 0.1
mixing_D_limit_for_log = 1d-10

! Overshooting
overshoot_f_above_burn_h_core = 0.020
overshoot_f0_above_burn_h_core = 0.001
D_mix_ov_limit = 1d0

! atmosphere boundary conditions

which_atm_option = 'photosphere_tables'
atm_switch_to_grey_as_backup = .true.
! parameters for Paczynski_grey
Paczynski_atm_R_surf_errtol = 1d-4
create_atm_max_step_size = 0.01

! mass gain or loss

mdot_omega_power = 0.43
max_rotational_mdot_boost = 1d4
hot_wind_scheme = 'Dutch'
Dutch_scaling_factor = 1d0
Dutch_wind_lowT_scheme = 'van Loon'
mass_change_full_on_dt = 3.15d8
mass_change_full_off_dt = 3.15d7

! mesh adjustment

```

```

! Initial setting for mesh, but for the 3rd run,
I use inlist_zoom.

use_other_mesh_functions = .true.

T_function2_weight = 100
T_function2_param = 18d4

xtra_coef_above_xtrans = 0.5
xtra_coef_below_xtrans = 0.5
xtra_dist_above_xtrans = 0.4
xtra_dist_below_xtrans = 0.4

mesh_dlog_pp_dlogP_extra = 0.20
mesh_dlog_cno_dlogP_extra = 0.20

mesh_dlog_3alf_dlogP_extra = 0.20
mesh_dlog_burn_c_dlogP_extra = 0.20
mesh_dlog_burn_n_dlogP_extra = 0.20
mesh_dlog_burn_o_dlogP_extra = 0.20

! timestep controls
dX_nuc_drop_limit = 5d-4
dX_nuc_drop_hard_limit = 1d-3

!nuclear reaction controls
default_net_name = 'cno_extras.net'

! element diffusion
do_element_diffusion = .false.
diffusion_dt_limit = 3.15d7

! opacity controls
use_Type2_opacities = .false.
Zbase = 2d-2

! asteroseismology controls

! for calculations of delta_nu and nu_max
get_delta_nu_from_scaled_solar = .true.
nu_max_sun = 3100d0
delta_nu_sun = 135d0
Teff_sun = 5777d0

! eps_grav
use_lnS_for_eps_grav = .true.
report_ierr = .false.

report_why_dt_limits = .false.

! Brunt

calculate_Brunt_N2 = .true.
num_cells_for_smooth_brunt_B = 3
use_brunt_gradmuX_form = .false.
/

Mesh adjustments are given by inlist_zoom:

&star_job

/

&controls

!max star age
max_age = 700d7

! mesh adjustment
mesh_delta_coeff = 0.5
max_allowed_nz = 2000000
okay_to_remesh = .true.

! radius gradient
R_function_weight = 1!0
R_function_param = 1d-4
R_function2_weight = 1000!10
R_function2_param1 = 0.8!1000
R_function2_param2 = 0.7!0

xtra_coef_above_xtrans = 0.1
xtra_coef_below_xtrans = 0.1
xtra_dist_above_xtrans = 0.5
xtra_dist_below_xtrans = 0.5
mesh_logX_species(1) = 'h1'
mesh_logX_min_for_extra(1) = -6
mesh_dlogX_dlogP_extra(1) = 0.1
mesh_dlogX_dlogP_full_on(1) = 2
mesh_dlogX_dlogP_full_off(1) = 1

mesh_logX_species(2) = 'he4'
mesh_logX_min_for_extra(2) = -6
mesh_dlogX_dlogP_extra(2) = 0.1
mesh_dlogX_dlogP_full_on(2) = 2
mesh_dlogX_dlogP_full_off(2) = 1

xtra_coef_czb_full_on = 1d0
xtra_coef_czb_full_off = 1d0

xtra_coef_a_l_nb_czb = 0.1
xtra_coef_a_l_hb_czb = 0.1
xtra_coef_a_l_heb_czb = 0.1

```

```

xtra_coef_a_l_zb_czb = 0.1

xtra_coef_b_l_nb_czb = 0.1
xtra_coef_b_l_hb_czb = 0.1
xtra_coef_b_l_heb_czb = 0.1
xtra_coef_b_l_zb_czb = 0.1

xtra_coef_a_u_nb_czb = 0.1
xtra_coef_a_u_hb_czb = 0.1
xtra_coef_a_u_heb_czb = 0.1
xtra_coef_a_u_zb_czb = 0.1

xtra_coef_b_u_nb_czb = 0.1
xtra_coef_b_u_hb_czb = 0.1
xtra_coef_b_u_heb_czb = 0.1
xtra_coef_b_u_zb_czb = 0.1

xtra_dist_a_l_nb_czb = 0.5
xtra_dist_a_l_hb_czb = 0.5
xtra_dist_a_l_heb_czb = 0.5
xtra_dist_a_l_zb_czb = 0.5

xtra_dist_b_l_nb_czb = 0.5
xtra_dist_b_l_hb_czb = 0.5
xtra_dist_b_l_heb_czb = 0.5
xtra_dist_b_l_zb_czb = 0.5

xtra_dist_a_u_nb_czb = 0.5
xtra_dist_a_u_hb_czb = 0.5
xtra_dist_a_u_heb_czb = 0.5
xtra_dist_a_u_zb_czb = 0.5

xtra_dist_b_u_nb_czb = 0.5
xtra_dist_b_u_hb_czb = 0.5
xtra_dist_b_u_heb_czb = 0.5
xtra_dist_b_u_zb_czb = 0.5

xtra_coef_os_full_on = 1d0
xtra_coef_os_full_off = 1d0

xtra_coef_os_above_nonburn = 0.1
xtra_coef_os_below_nonburn = 0.1
xtra_coef_os_above_burn_h = 0.1
xtra_coef_os_below_burn_h = 0.1
xtra_coef_os_above_burn_he = 0.1
xtra_coef_os_below_burn_he = 0.1
xtra_coef_os_above_burn_z = 0.1
xtra_coef_os_below_burn_z = 0.1

xtra_dist_os_above_nonburn = 0.5
xtra_dist_os_below_nonburn = 0.5
xtra_dist_os_above_burn_h = 0.5
xtra_dist_os_below_burn_h = 0.5
xtra_dist_os_above_burn_he = 0.5
xtra_dist_os_below_burn_he = 0.5
xtra_dist_os_above_burn_z = 0.5
xtra_dist_os_below_burn_z = 0.5

convective_bdy_weight = 0
convective_bdy_dq_limit = 1d-4
convective_bdy_min_dt_yrs = 1d-3

okay_to_remesh = .true.

remesh_dt_limit = -1
remesh_log_L_nuc_burn_min = -50

/ ! end of controls namelist

```

REFERENCES

- Aerts, C., Molenberghs, G., Kenward, M. G., & Neiner, C. 2014, *ApJ*, 781, 88, doi: [10.1088/0004-637X/781/2/88](https://doi.org/10.1088/0004-637X/781/2/88)
- Alongi, M., Bertelli, G., Bressan, A., & Chiosi, C. 1991, *A&A*, 244, 95
- Belkacem, K., Samadi, R., Goupil, M. J., et al. 2009, *A&A*, 494, 191, doi: [10.1051/0004-6361/200810827](https://doi.org/10.1051/0004-6361/200810827)
- Brott, I., Evans, C. J., Hunter, I., et al. 2011, *A&A*, 530, A116, doi: [10.1051/0004-6361/201016114](https://doi.org/10.1051/0004-6361/201016114)
- Brown, T. M., Christensen-Dalsgaard, J., Dziembowski, W. A., et al. 1989, *ApJ*, 343, 526, doi: [10.1086/167727](https://doi.org/10.1086/167727)
- Brüggen, M., & Hillebrandt, W. 2001, *MNRAS*, 320, 73, doi: [10.1046/j.1365-8711.2001.03951.x](https://doi.org/10.1046/j.1365-8711.2001.03951.x)
- Busso, M., Wasserburg, G. J., Nollett, K. M., & Calandra, A. 2007, *ApJ*, 671, 802, doi: [10.1086/522616](https://doi.org/10.1086/522616)
- Cantiello, M., & Langer, N. 2010, *A&A*, 521, A9, doi: [10.1051/0004-6361/201014305](https://doi.org/10.1051/0004-6361/201014305)
- Cantiello, M., Mankovich, C., Bildsten, L., Christensen-Dalsgaard, J., & Paxton, B. 2014, *The Astrophysical Journal*, 788, 93, doi: [10.1088/0004-637x/788/1/93](https://doi.org/10.1088/0004-637x/788/1/93)
- Canto Martins, B., LEBRE, A., PALACIOS, A., et al. 2011, *Astronomy & Astrophysics - ASTRON ASTROPHYS*, 527, doi: [10.1051/0004-6361/201015015](https://doi.org/10.1051/0004-6361/201015015)

- Ceillier, T., Eggenberger, P., García, R. A., & Mathis, S. 2013, *A&A*, 555, A54, doi: [10.1051/0004-6361/201321473](https://doi.org/10.1051/0004-6361/201321473)
- Chang, E., & Garaud, P. 2021, *MNRAS*, 506, 4914, doi: [10.1093/mnras/stab1927](https://doi.org/10.1093/mnras/stab1927)
- Charbonnel, C. 1994, *A&A*, 282, 811
- Charbonnel, C., & Lagarde, N. 2010, *A&A*, 522, A10, doi: [10.1051/0004-6361/201014432](https://doi.org/10.1051/0004-6361/201014432)
- Charbonnel, C., & Talon, S. 2007, in *American Institute of Physics Conference Series*, Vol. 948, *Unsolved Problems in Stellar Physics: A Conference in Honor of Douglas Gough*, ed. R. J. Stancliffe, G. Houdek, R. G. Martin, & C. A. Tout, 15–26, doi: [10.1063/1.2818965](https://doi.org/10.1063/1.2818965)
- Charbonnel, C., & Zahn, J.-P. 2007, *A&A*, 467, L15, doi: [10.1051/0004-6361:20077274](https://doi.org/10.1051/0004-6361:20077274)
- Charpinet, S., Van Grootel, V., Fontaine, G., et al. 2011, *A&A*, 530, A3, doi: [10.1051/0004-6361/201016412](https://doi.org/10.1051/0004-6361/201016412)
- Chieffi, A., & Limongi, M. 2013, *ApJ*, 764, 21, doi: [10.1088/0004-637X/764/1/21](https://doi.org/10.1088/0004-637X/764/1/21)
- Christensen-Dalsgaard, J., Monteiro, M. J. P. F. G., Rempel, M., & Thompson, M. J. 2011, *Monthly Notices of the Royal Astronomical Society*, 414, 1158, doi: [10.1111/j.1365-2966.2011.18460.x](https://doi.org/10.1111/j.1365-2966.2011.18460.x)
- Deheuvels, S. 2020, *Probing core overshooting using asteroseismology*. <https://arxiv.org/abs/2001.04178>
- Eddington, A. S. 1925, *The Observatory*, 48, 73
- Eggenberger, P., Meynet, G., Maeder, A., et al. 2008, *Ap&SS*, 316, 43, doi: [10.1007/s10509-007-9511-y](https://doi.org/10.1007/s10509-007-9511-y)
- Eggenberger, P., Montalbán, J., & Miglio, A. 2012, *A&A*, 544, L4, doi: [10.1051/0004-6361/201219729](https://doi.org/10.1051/0004-6361/201219729)
- Eggleton, P. P., Dearborn, D. S. P., & Lattanzio, J. C. 2006, *Science*, 314, 1580, doi: [10.1126/science.1133065](https://doi.org/10.1126/science.1133065)
- Endal, A. S., & Sofia, S. 1976, *ApJ*, 210, 184, doi: [10.1086/154817](https://doi.org/10.1086/154817)
- Garaud, P. 2020, *ApJ*, 901, 146, doi: [10.3847/1538-4357/ab9c99](https://doi.org/10.3847/1538-4357/ab9c99)
- García Lopez, R. J., & Spruit, H. C. 1991, *ApJ*, 377, 268, doi: [10.1086/170356](https://doi.org/10.1086/170356)
- Giammichele, N., Charpinet, S., Fontaine, G., et al. 2018, *Nature*, 554, 73, doi: [10.1038/nature25136](https://doi.org/10.1038/nature25136)
- Gies, D. R., & Lambert, D. L. 1992, *ApJ*, 387, 673, doi: [10.1086/171116](https://doi.org/10.1086/171116)
- Goldreich, P., & Schubert, G. 1967, *ApJ*, 150, 571, doi: [10.1086/149360](https://doi.org/10.1086/149360)
- Heger, A., & Langer, N. 2000, *ApJ*, 544, 1016, doi: [10.1086/317239](https://doi.org/10.1086/317239)
- Heger, A., Langer, N., & Woosley, S. E. 2000, *The Astrophysical Journal*, 528, 368–396, doi: [10.1086/308158](https://doi.org/10.1086/308158)
- Heger, A., Woosley, S. E., & Spruit, H. C. 2005, *ApJ*, 626, 350, doi: [10.1086/429868](https://doi.org/10.1086/429868)
- Herrero, A., Kudritzki, R. P., Vilchez, J. M., et al. 1992, *A&A*, 261, 209
- Herwig, F. 2000, *A&A*, 360, 952, <https://arxiv.org/abs/astro-ph/0007139>
- Hirschi, R. 2007, *A&A*, 461, 571, doi: [10.1051/0004-6361:20065356](https://doi.org/10.1051/0004-6361:20065356)
- Hurlburt, N. E., Toomre, J., & Massaguer, J. M. 1986, *The Astrophysical Journal*, 311, 563
- Kippenhahn, R., Meyer-Hofmeister, E., & Thomas, H. C. 1970, *A&A*, 5, 155
- Kraft, R. P. 1994, *PASP*, 106, 553, doi: [10.1086/133416](https://doi.org/10.1086/133416)
- Kulenthirarajah, L., & Garaud, P. 2018, *ApJ*, 864, 107, doi: [10.3847/1538-4357/aad5e8](https://doi.org/10.3847/1538-4357/aad5e8)
- Kumar, P., Talon, S., & Zahn, J.-P. 1999, *ApJ*, 520, 859, doi: [10.1086/307464](https://doi.org/10.1086/307464)
- Lagarde, N., Charbonnel, C., Decressin, T., & Hagelberg, J. 2011, *A&A*, 536, A28, doi: [10.1051/0004-6361/201117739](https://doi.org/10.1051/0004-6361/201117739)
- Lecoanet, D., & Quataert, E. 2013, *Monthly Notices of the Royal Astronomical Society*, 430, 2363, doi: [10.1093/mnras/stt055](https://doi.org/10.1093/mnras/stt055)
- Liubimkov, L. S. 1975, *Soviet Astronomy Letters*, 1, 226
- . 1977, *Astrofizika*, 13, 139, doi: [10.1007/BF01003156](https://doi.org/10.1007/BF01003156)
- Lyubimkov, L. S. 1989, *Astrofizika*, 30, 99
- . 1996, *Ap&SS*, 243, 329, doi: [10.1007/BF00644704](https://doi.org/10.1007/BF00644704)
- Maeder, A. 1976, *A&A*, 47, 389
- . 2003, *A&A*, 399, 263, doi: [10.1051/0004-6361:20021731](https://doi.org/10.1051/0004-6361:20021731)
- Maeder, A., & Meynet, G. 2000, *Annual Review of Astronomy and Astrophysics*, 38, 143–190, doi: [10.1146/annurev.astro.38.1.143](https://doi.org/10.1146/annurev.astro.38.1.143)
- Maeder, A., & Meynet, G. 2005, *A&A*, 440, 1041, doi: [10.1051/0004-6361:20053261](https://doi.org/10.1051/0004-6361:20053261)
- Maeder, A., & Zahn, J.-P. 1998, *A&A*, 334, 1000
- Marques, J. P., Goupil, M. J., Lebreton, Y., et al. 2013, *A&A*, 549, A74, doi: [10.1051/0004-6361/201220211](https://doi.org/10.1051/0004-6361/201220211)
- Martins, F., Simón-Díaz, S., Barbá, R. H., Gamen, R. C., & Ekström, S. 2017, *A&A*, 599, A30, doi: [10.1051/0004-6361/201629548](https://doi.org/10.1051/0004-6361/201629548)
- Mathis, S., Palacios, A., & Zahn, J. P. 2004, *A&A*, 425, 243, doi: [10.1051/0004-6361:20040279](https://doi.org/10.1051/0004-6361:20040279)
- Mathis, S., Prat, V., Amard, L., et al. 2018, *A&A*, 620, A22, doi: [10.1051/0004-6361/201629187](https://doi.org/10.1051/0004-6361/201629187)
- Matias, J., & Zahn, J. P. 1997, *Sounding Solar and Stellar Interiors: Proceedings of the 181st Symposium of the International Astronomical Union Held in Nice, France, September 30 - October 3, 1996*, ed. J. Provost & F. Schmider (Kluwer). <https://books.google.ci/books?id=e1GpAQAACAAJ>
- Montalbán, J. 1994, *A&A*, 281, 421
- Montalbán, J., & Schatzman, E. 1996, *A&A*, 305, 513
- Montalbán, J., & Schatzman, E. 2000, *A&A*, 354, 943

- Montalbán, J., & Schatzman, E. 1993, *International Astronomical Union Colloquium*, 137, 281–283, doi: [10.1017/S0252921100017929](https://doi.org/10.1017/S0252921100017929)
- Monteiro, M. J. P. F. G., Christensen-Dalsgaard, J., & Thompson, M. J. 2000, *Monthly Notices of the Royal Astronomical Society*, 316, 165, doi: [10.1046/j.1365-8711.2000.03471.x](https://doi.org/10.1046/j.1365-8711.2000.03471.x)
- Noels, A., Montalban, J., Miglio, A., Godart, M., & Ventura, P. 2010, *Ap&SS*, 328, 227, doi: [10.1007/s10509-009-0203-7](https://doi.org/10.1007/s10509-009-0203-7)
- Nordhaus, J., Busso, M., Wasserburg, G. J., Blackman, E. G., & Palmerini, S. 2008, *ApJL*, 684, L29, doi: [10.1086/591963](https://doi.org/10.1086/591963)
- Ouazzani, R. M., Marques, J. P., Goupil, M. J., et al. 2019, *A&A*, 626, A121, doi: [10.1051/0004-6361/201832607](https://doi.org/10.1051/0004-6361/201832607)
- Paczyński, B. 1973, *AcA*, 23, 191
- Palacios, A., Charbonnel, C., Talon, S., & Siess, L. 2006, *A&A*, 453, 261, doi: [10.1051/0004-6361:20053065](https://doi.org/10.1051/0004-6361:20053065)
- Palacios, A., Talon, S., Charbonnel, C., & Forestini, M. 2003, *A&A*, 399, 603, doi: [10.1051/0004-6361:20021759](https://doi.org/10.1051/0004-6361:20021759)
- Park, J., Prat, V., & Mathis, S. 2020, *A&A*, 635, A133, doi: [10.1051/0004-6361/201936863](https://doi.org/10.1051/0004-6361/201936863)
- Park, J., Prat, V., Mathis, S., & Bugnet, L. 2021, *A&A*, 646, A64, doi: [10.1051/0004-6361/202038654](https://doi.org/10.1051/0004-6361/202038654)
- Paxton, B., Bildsten, L., Dotter, A., et al. 2011, *ApJS*, 192, 3, doi: [10.1088/0067-0049/192/1/3](https://doi.org/10.1088/0067-0049/192/1/3)
- Paxton, B., Cantiello, M., Arras, P., et al. 2013, *ApJS*, 208, 4, doi: [10.1088/0067-0049/208/1/4](https://doi.org/10.1088/0067-0049/208/1/4)
- Paxton, B., Marchant, P., Schwab, J., et al. 2015, *ApJS*, 220, 15, doi: [10.1088/0067-0049/220/1/15](https://doi.org/10.1088/0067-0049/220/1/15)
- Paxton, B., Schwab, J., Bauer, E. B., et al. 2018, *ApJS*, 234, 34, doi: [10.3847/1538-4365/aaa5a8](https://doi.org/10.3847/1538-4365/aaa5a8)
- Paxton, B., Smolec, R., Schwab, J., et al. 2019, *ApJS*, 243, 10, doi: [10.3847/1538-4365/ab2241](https://doi.org/10.3847/1538-4365/ab2241)
- Pedersen, M. G., Aerts, C., Pápics, P. I., & Rogers, T. M. 2018, *Astronomy & Astrophysics*, 614, A128, doi: [10.1051/0004-6361/201732317](https://doi.org/10.1051/0004-6361/201732317)
- Pedersen, M. G., Aerts, C., Pápics, P. I., et al. 2021, *Nature Astronomy*, 5, 715–722, doi: [10.1038/s41550-021-01351-x](https://doi.org/10.1038/s41550-021-01351-x)
- Pilachowski, C. A., Sneden, C., & Booth, J. 1993, *ApJ*, 407, 699, doi: [10.1086/172551](https://doi.org/10.1086/172551)
- Pinçon, C., Belkacem, K., & Goupil, M. J. 2016, *A&A*, 588, A122, doi: [10.1051/0004-6361/201527663](https://doi.org/10.1051/0004-6361/201527663)
- Pinsonneault, M. H., Kawaler, S. D., Sofia, S., & Demarque, P. 1989, *ApJ*, 338, 424, doi: [10.1086/167210](https://doi.org/10.1086/167210)
- Prat, V., & Lignières, F. 2013, *A&A*, 551, L3, doi: [10.1051/0004-6361/201220577](https://doi.org/10.1051/0004-6361/201220577)
- Prat, V., & Mathis, S. 2021, *A&A*, 649, A62, doi: [10.1051/0004-6361/202039281](https://doi.org/10.1051/0004-6361/202039281)
- Press, W. H. 1981, *ApJ*, 245, 286, doi: [10.1086/158809](https://doi.org/10.1086/158809)
- Ratnasingam, R. P. 2020, PhD thesis, Newcastle University
- Ratnasingam, R. P., Edelmann, P. V. F., & Rogers, T. M. 2018, *Monthly Notices of the Royal Astronomical Society*, 482, 5500, doi: [10.1093/mnras/sty3086](https://doi.org/10.1093/mnras/sty3086)
- . 2020, *Monthly Notices of the Royal Astronomical Society*, 497, 4231, doi: [10.1093/mnras/staa2296](https://doi.org/10.1093/mnras/staa2296)
- Rogers, T. M., Glatzmaier, G. A., & Jones, C. A. 2006, *The Astrophysical Journal*, 653, 765, doi: [10.1086/508482](https://doi.org/10.1086/508482)
- Rogers, T. M., Lin, D. N. C., McElwaine, J. N., & Lau, H. H. B. 2013, *ApJ*, 772, 21, doi: [10.1088/0004-637X/772/1/21](https://doi.org/10.1088/0004-637X/772/1/21)
- Rogers, T. M., & McElwaine, J. N. 2017, *ApJL*, 848, L1, doi: [10.3847/2041-8213/aa8d13](https://doi.org/10.3847/2041-8213/aa8d13)
- Samadi, R., Belkacem, K., Goupil, M. J., et al. 2010, *Ap&SS*, 328, 253, doi: [10.1007/s10509-009-0215-3](https://doi.org/10.1007/s10509-009-0215-3)
- Schröder, K.-P., Pols, O. R., & Eggleton, P. P. 1997, *Monthly Notices of the Royal Astronomical Society*, 285, 696, doi: [10.1093/mnras/285.4.696](https://doi.org/10.1093/mnras/285.4.696)
- Siess, L., Dufour, E., & Forestini, M. 2000, *A&A*, 358, 593, <https://arxiv.org/abs/astro-ph/0003477>
- Spruit, H. C. 2002, *A&A*, 381, 923, doi: [10.1051/0004-6361:20011465](https://doi.org/10.1051/0004-6361:20011465)
- Spruit, H. C., Knobloch, E., & Roxburgh, I. W. 1983, *Nature*, 304, 520, doi: [10.1038/304520a0](https://doi.org/10.1038/304520a0)
- Stancliffe, R. J. 2010, *MNRAS*, 403, 505, doi: [10.1111/j.1365-2966.2009.16150.x](https://doi.org/10.1111/j.1365-2966.2009.16150.x)
- Talon, S., & Charbonnel, C. 2005, *Astronomy & Astrophysics*, 440, 981–994, doi: [10.1051/0004-6361:20053020](https://doi.org/10.1051/0004-6361:20053020)
- Talon, S., & Zahn, J. P. 1997, *A&A*, 317, 749, <https://arxiv.org/abs/astro-ph/9609010>
- Vescovi, D., Cristallo, S., Busso, M., & Liu, N. 2020, *The Astrophysical Journal*, 897, L25, doi: [10.3847/2041-8213/ab9fa1](https://doi.org/10.3847/2041-8213/ab9fa1)
- Walborn, N. R. 1976, *ApJ*, 205, 419, doi: [10.1086/154292](https://doi.org/10.1086/154292)
- Zahn, J. P. 1991, *A&A*, 252, 179
- . 1992, *A&A*, 265, 115
- Zahn, J. P. 1994, in *Evolution of Massive Stars*, 285–297
- Zahn, J. P., Talon, S., & Matias, J. 1997, *A&A*, 322, 320, <https://arxiv.org/abs/astro-ph/9611189>